J. Fluid Mech. (1992), *vol.* 245, *pp.* 155–173

Convection in a rotating cylindrical annulus Part 3. Vacillating and spatially modulated flows

By M. SCHNAUBELT AND F. H. BUSSE
Institute of Physics, University of Bayreuth, D-8580 Bayreuth, Germany

(Received 9 March 1992)

The problem of convection driven by radial buoyancy in a rotating cylindrical annulus with conical end surfaces represents one of the basic models of rotating fluid dynamics with applications to convection in planets and stars. Although only two-dimensional equations govern the flow in the limit of high rotation rates, a surprising variety of different states of motion can be found. In this paper earlier numerical work is extended by the consideration of rigid boundary conditions at the cylindrical walls and by a study of spatially modulated convection. Of particular interest is the case of curved conical end surfaces which appears to promote the formation of separate cylindrical convection layers.

1. Introduction

Convection driven by thermal buoyancy in rotating systems is of basic interest in fluid dynamics for two reasons. On the one hand it represents a fundamental process in planetary and stellar atmospheres. Because of the complications arising from the varying angle between the vectors of gravity and rotation in the spherical geometry, the study of fluid layers with a fixed angle between the two vectors has been preferred. In particular cases with a vertical or a horizontal axis of rotation have been investigated. These studies have led to a second motivation for the rising interest in the problem. It has turned out that convection in rotating layers exhibits unusual features in its nonlinear dynamics. In the case of a vertical axis of rotation, the evolution of the Küppers–Lortz instability leads to an interesting case of phase turbulence (Küppers & Lortz 1969; Busse & Clever 1979; Busse & Heikes 1980; Busse 1984). In the case of a layer with a horizontal axis of rotation a sequence of transitions to time-dependent states with increasing complexity has been found (Or & Busse 1987, hereinafter referred to as OB87) while the convection flow preserves its dependence on only two spatial coordinates. This latter property makes it an ideal problem for investigation by numerical methods and has motivated the analysis presented in this paper.

Convection in a layer heated from below with a horizontal axis of rotation can be easily realized in the laboratory through the use of the centrifugal force as the effective gravity. Two coaxial cylinders, the outer one heated, the inner one cooled, are rotated rigidly about their common axis. This axis is oriented vertically in the laboratory frame of reference in order to avoid fluctuating effects from the Earth's gravity in the rotating system. When the temperature difference across the fluid-filled annular gap between the cylinders is sufficiently large, convection driven by centrifugal buoyancy sets in. The preferred convection flow assumes the form of rolls aligned with the axis of rotation (Busse 1970). In the limit of a small gap width the

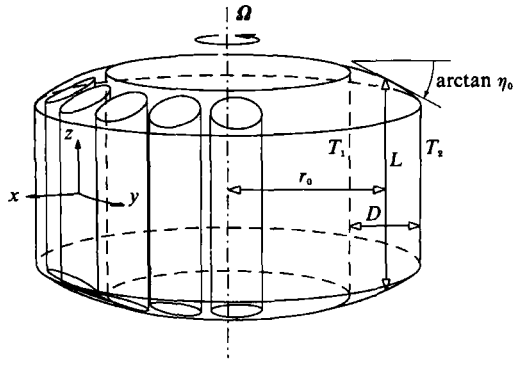

FIGURE 1. Geometric configuration of the rotating cylindrical annulus. The angle χ equals arctan η_0.

plane-layer approximation can be used. In this case the convection rolls are identical to those in a non-rotating Rayleigh–Bénard layer as long as the end boundaries are parallel and sufficiently distant such that the Ekman layers at these boundaries have a minimal effect. This property is due to the geostrophic equilibrium satisfied by the rolls which ensures that the Coriolis force is balanced entirely by the pressure gradient. The more interesting case is obtained when conical end boundaries are assumed such that the depth of the fluid in the direction of the axis of rotation varies with the distance from the axis. The geostrophic balance cannot be satisfied completely in this case with the consequence of Rossby-wave-like dynamics of the convection rolls. At the same time the azimuthal wavenumber of the preferred convection roll increases in order to optimize the release of potential energy. Because the influence of the boundary conditions at the cylindrical sidewalls disappears in the limit of high rotation rates, the annulus model can be applied with minor modifications to the case of a sphere (Busse 1970, 1982, 1986). We thus expect that much of the dynamics that can be studied on the basis of two-dimensional equations in the case of the cylindrical annulus will be representative for the more complex situation of convection in rotating spheres.

The goal of this paper is to give a more detailed description of some of the transitions found in the analysis of OB87 and to focus in particular on the modulational instabilities of the singly periodic roll pattern. After formulating the mathematical problem and the method of solution in §2 we turn to the analysis of the stability of steadily drifting rolls in §3. In §4 vacillating convection rolls of various kind are investigated and in §5 the interesting case of curved conical end surfaces is considered. The paper closes with an outlook on applications to the dynamics in the major planets.

2. Formulation of the mathematical problem and method of analysis

We consider a fluid-filled cylindrical annulus of height L rotating about its axis of symmetry with the constant angular velocity Ω. The mean radius of the angular gap is r_0 and its thickness is D. The cylindrical walls are kept at the temperatures T_1 and T_2. Buoyancy-driven thermal convection occurs through the action of the centrifugal force when the temperature T_2 at the outer cylindrical wall exceeds T_1 by a sufficiently large amount. For a dimensionless description we introduce D as lengthscale, D^2/ν as timescale where ν is the kinematic viscosity, and $(T_2-T_1)P$ as

temperature scale where P is the Prandtl number. Assuming the small-gap approximation, $D \ll r_0$, we introduce a Cartesian system of coordinates with the (x, y, z)-coordinates pointing in the radial, azimuthal and axial directions, respectively, as shown in figure 1. The end surfaces are assumed to be symmetric with respect to the equatorial plane with

$$\eta = \eta_0(1+\epsilon x) \tag{2.1}$$

representing the tangent of the angle of inclination χ. The velocity field of convection can be written in the form

$$\boldsymbol{v} = \boldsymbol{\nabla} \times \boldsymbol{k}\psi(x, y, t) + \hat{\boldsymbol{v}}, \tag{2.2}$$

where $\boldsymbol{k}$ is the axial unit vector and $\hat{\boldsymbol{v}}$ represents the ageostrophic component of $\boldsymbol{v}$ which is of the order η_0 for small values of this parameter. As shown by Busse (1970, 1986) the following dimensionless equations for ψ and for the deviation θ of the temperature from the static distribution are obtained for small η_0:

$$\left(\frac{\partial}{\partial t}+\frac{\partial}{\partial y}\psi\frac{\partial}{\partial x}-\frac{\partial}{\partial x}\psi\frac{\partial}{\partial y}\right)\Delta_2\psi-\eta^*(1+\epsilon x)\frac{\partial}{\partial y}\psi-\Delta_2^2\psi+R\frac{\partial}{\partial y}\theta=0, \tag{2.3a}$$

$$P\left(\frac{\partial}{\partial t}+\frac{\partial}{\partial y}\psi\frac{\partial}{\partial x}-\frac{\partial}{\partial x}\psi\frac{\partial}{\partial y}\right)\theta+\frac{\partial}{\partial y}\psi-\Delta_2\theta=0, \tag{2.3b}$$

where the Rayleigh number R, the Prandtl number P, and the Coriolis parameter η^* are defined by

$$R \equiv \frac{\gamma D^3(T_2-T_1)\Omega^2 r_0}{\nu\kappa}, \quad P \equiv \frac{\nu}{\kappa}, \quad \eta^* \equiv \frac{4\eta_0\Omega D^3}{\nu L}. \tag{2.4}$$

The coefficient γ of thermal expansion and the thermal diffusivity κ have been used in these definitions. The operator Δ_2 represents the two-dimensional Laplacian in the (x, y)-plane. The parameter η^* is analogous to the parameter β of the β-plane approximation used in meteorology. The corresponding term in (2.3a) describes the effect of the stretching of vortex lines as they change their distance from the axis. In spite of the smallness of η_0, η^* is typically a large parameter since we are interested in the limit of high rotation rates Ω.

For the solution of (2.3) we introduce the Galerkin representation,

$$\psi = \sum_{mn}\left[\hat{a}_{mn}\cos n\alpha(y-ct)+\check{a}_{mn}\sin n\alpha(y-ct)\right]g_m(x)+F(x), \tag{2.5a}$$

$$\theta = \sum_{mn}\left[\hat{b}_{mn}\cos n\alpha(y-ct)+\check{b}_{mn}\sin n\alpha(y-ct)\right]\sin m\pi(x+\tfrac{1}{2}), \tag{2.5b}$$

where the subscripts m and n run through all positive integers and where in addition the terms with $\hat{a}_{m0}$, $\hat{b}_{m0}$ are included. $F(x)$ denotes an additional term which is needed to satisfy the boundary conditions for the mean zonal flow. Two different types of conditions at the boundaries $x = \pm\frac{1}{2}$ will be considered and corresponding choices for the functions $g_m(x)$ will be made. In all cases the temperature θ vanishes at the boundaries.

For applications to laboratory experiments no-slip conditions are of special interest,

$$g_m(x) = (\mathrm{d}/\mathrm{d}x)\,g_m(x) = 0 \quad \text{at} \quad x = \pm\tfrac{1}{2}. \tag{2.6a}$$

A complete set of function satisfying those conditions has been introduced by Chandrasekhar (1961),

$$g_m(x) \equiv \begin{cases} \dfrac{\cosh \kappa_m x}{\cosh \kappa_m/2} - \dfrac{\cos \kappa_m x}{\cos \kappa_m/2} & \text{for odd } m \\ \dfrac{\sinh \kappa_m x}{\sinh \kappa_m/2} - \dfrac{\sin \kappa_m x}{\sin \kappa_m/2} & \text{for even } m \end{cases} \tag{2.6b}$$

and a table for the values κ_m can be found in that reference. Since no mean pressure gradient in the y-direction is allowed, but an average zonal flow must be admitted, the y-average of ψ may have finite values at $x = \pm\frac{1}{2}$. The function

$$F(x) \equiv \hat{a}(x^3 - \tfrac{3}{4}x) \tag{2.6c}$$

is a solution of the homogeneous equation $\partial^4\psi/\partial x^4 = 0$ and a constant $\hat{a}$ is determined by the condition of vanishing mean azimuthal pressure gradient,

$$\hat{a} = -\frac{1}{6}\int_{-\frac{1}{2}}^{\frac{1}{2}} \sum_m g_m'''(x)\,\hat{a}_{m0}\,\mathrm{d}x. \tag{2.6d}$$

The solution for $F(x) \equiv 0$ would correspond to the case when a barrier at $y = y_0$ would support a mean pressure gradient together with the requirement of a vanishing azimuthal mean flow.

Another case of interest is stress-free boundary conditions for the fluctuating component of the velocity field with the possibility of a periodic continuation of the layer. The complete set of functions corresponding to the conditions

$$g_m(x) = (\mathrm{d}^2/\mathrm{d}x^2)\,g_m(x) = 0 \quad \text{at} \quad x = \pm\tfrac{1}{2} \tag{2.7a}$$

is given by

$$g_m(x) \equiv \sin m\pi(x + \tfrac{1}{2}). \tag{2.7b}$$

The periodic continuation of the layer requires that the mean azimuthal flow U satisfies the conditions

$$(\partial/\partial x)\,U(-\tfrac{1}{2}) = (\partial/\partial x)\,U(+\tfrac{1}{2}), \quad U(-\tfrac{1}{2}) = U(+\tfrac{1}{2}), \tag{2.7c}$$

and leads to the prescription

$$F(x) \equiv (x^2 - \tfrac{1}{4}) \sum_{m=\text{odd}} m\pi\,\hat{a}_{m0}. \tag{2.7d}$$

The boundary conditions (2.7), motivated by a model of convection in the Jovian atmosphere, were introduced by OB87. We shall refer to this case as the case of periodic boundary conditions. Conditions (2.7a, b) without the imposition of a periodic mean flow have been used by Schnaubelt (1992) and by Brummell & Hart (1992). The latter paper is restricted to the case $P = 1$, but emphasizes higher Rayleigh numbers than those used by Schnaubelt (1992) and in the present analysis.

Solutions (2.5) in the form of stationarily drifting rolls or columns can be obtained for constant coefficients $\hat{a}_{mn}, \check{a}_{mn}, \hat{b}_{mn}, \check{b}_{mn}$. An algebraic system of equations for these coefficients is obtained after the representation (2.5) has been introduced into (2.3) and these equations have been multiplied by the expansion functions and averaged over the fluid domain. Because of the translation invariance in the y-direction we can fix the phase of the solution by setting a coefficient, say $\check{a}_{11}$, equal to zero and using the corresponding equation for the determination of the phase velocity c. In order to obtain a numerical solution with a Newton–Raphson method we must truncate the system of equations. We shall neglect all coefficients and corresponding equations, with subscripts m, n satisfying

$$m + n > N_{\mathrm{T}}. \tag{2.8}$$

By changing N_T we can check the accuracy of the approximation.

The stability of the stationary solution of the form (2.5) can be studied through the superposition of infinitesimal disturbances,

$$\tilde{\psi} = \sum_{mn} \tilde{a}_{mn} \exp\{\mathrm{i}(n\alpha+d)(y-ct)+\sigma t\}\, g_m(x) + \tilde{F}(x,y,t), \tag{2.9a}$$

$$\tilde{\theta} = \sum_{mn} \tilde{b}_{mn} \exp\{\mathrm{i}(n\alpha+d)(y-ct)+\sigma t\} \sin m\pi(x+\tfrac{1}{2}), \tag{2.9b}$$

with

$$\tilde{F}(x,y,t) = \begin{cases} \tilde{a}(x^3-\frac{3}{4}x)\exp\{\sigma t\} & \text{for } d=0 \\ 0 & \text{for } d \neq 0, \end{cases} \tag{2.10a}$$

$$\tilde{a} = -\frac{1}{6}\int_{-\frac{1}{2}}^{\frac{1}{2}} \sum_m g_m'''(x)\, \tilde{a}_{m0}\, \mathrm{d}x \tag{2.10b}$$

in the case (2.6), and with the definition

$$\tilde{F}(x,y,t) = (x^2-\tfrac{1}{4}) \sum_{m=\text{odd}} m\pi \tilde{a}_{m0} \exp\{\mathrm{i}d(y-ct)+\sigma t\}. \tag{2.11}$$

in the case (2.7). For reasons of continuity the conditions (2.7*c*) for the mean flow have been extended to long-wavelength disturbances in (2.11), since d usually assumes rather small values. The corresponding condition (2.10*a*) does not cause any discontinuity since it represents the smooth transition from finite values of d to the case $d = 0$. The introduction of the ansatz (2.9) in the linearized equations yields a system of linear homogeneous equations with σ as eigenvalue. For a given stationary solution of the form (2.5) the eigenvalues σ are computed as functions of d and the value of σ with maximum real part σ_r is determined. Whenever this value is positive the stationary solution is unstable; otherwise it is regarded as stable. For given P and η^*, regions of stable stationary solutions can thus be determined in the (R,α)-plane.

Since the instabilities often grow with finite imaginary part σ_i of the eigenvalue σ, their evolution can be followed only by a forward integration in time. For this purpose the coefficients $\hat{a}_{mn}$, $\check{a}_{mn}$, $\hat{b}_{mn}$, $\check{b}_{mn}$ in (2.5) are assumed to be time dependent, and instead of the system of nonlinear algebraic equations a system of first-order differential equations in time must be solved. For this purpose a second-order Adams–Bashforth method, a fourth-order Runge–Kutta scheme, or a Crank–Nicolson method have been employed. Depending on the character of the evolving time-dependent solutions either one of the first two computationally less intensive methods or the latter method known for its numerical stability, have been used.

3. Stationary solutions and their instabilities

In the case without curvature, $\epsilon = 0$, the basic equations exhibit an additional symmetry and admit stationary solutions of the form (2.5) with the property

$$\hat{a}_{mn} = \check{a}_{mn} = \hat{b}_{mn} = \check{b}_{mn} = 0 \quad \text{for} \quad m+n = \text{odd}. \tag{3.1}$$

These solutions have been called symmetric thermal Rossby waves and are preferred at low Rayleigh numbers since they correspond to the strongest growing modes at the onset of convection. Because of the property (3.1) the disturbances of the form (2.1) separate into two classes, symmetric disturbances with vanishing coefficients $\tilde{a}_{mn}$, $\tilde{b}_{mn}$ for odd $m+n$ and anti-symmetric disturbances with vanishing coefficients

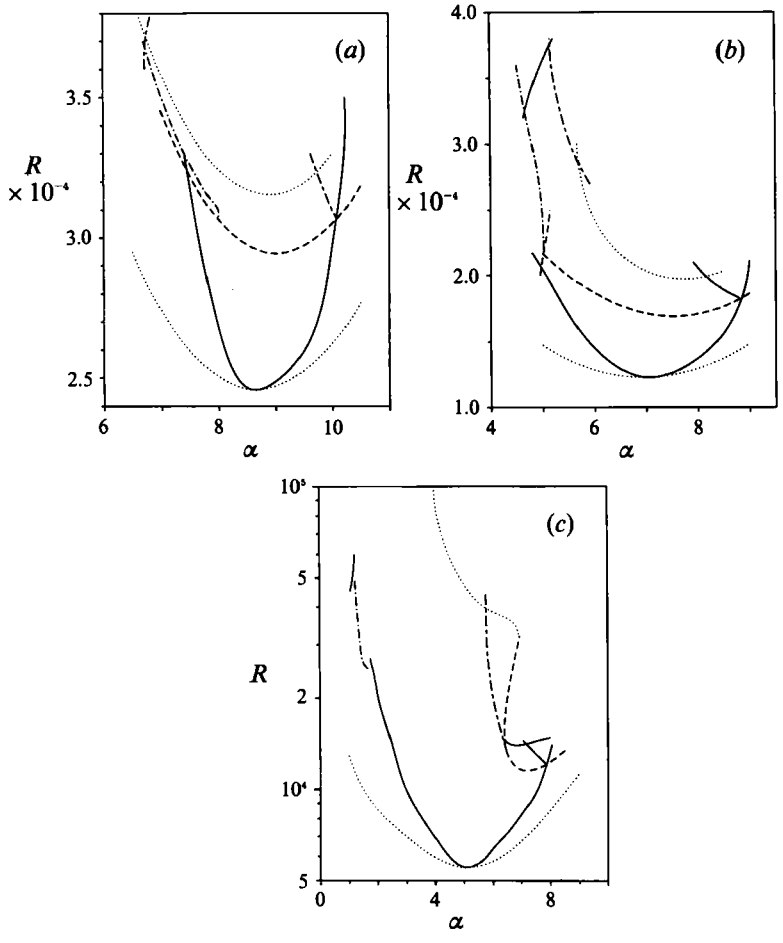

FIGURE 2. Stability regions of symmetric rolls (between solid and dashed lines) and of mean flow convection (between dashed and upper dotted lines) in the case of rigid boundaries with $P = 0.7$ for (*a*) $\eta^* = 2800$, (*b*) $\eta^* = 1600$ and (*c*) $\eta^* = 800$. The lower dotted line indicates the neutral curve for the onset of convection; solid, dash-dotted, and double-dashed curves indicate various sideband mechanisms of instability. In (*c*) the short dash – long dash curve on the right-hand side indicates the range of existence – at finite amplitudes – of the mean flow convection solution. The range between this curve and the single-dash curve thus indicates the regime in which the mean flow solution is subcritical in the parameter α.

for even $m+n$. Among the former disturbances are the sideband instabilities which limit the range of wavenumbers α for which the symmetric thermal Rossby waves are realizable. To the latter class of disturbances belong the mean flow instability and the vacillating instability.

A typical plot of the stability boundaries is shown in figure 2(*a*). Although rigid boundary conditions (2.6) have been assumed for these cases, the stability boundaries are remarkably similar to those shown in OB87 for the periodic case (2.7). After the onset of the mean flow solution this asymmetric form of convection remains stationary in the appropriately drifting frame of reference for a relatively small range of the Rayleigh number until it becomes unstable with respect to the onset of amplitude vacillations. The vacillation instability is typically associated with a small value of the Floquet parameter d, but growing disturbances also exist for $d = 0$, albeit at a somewhat higher Rayleigh number. The term 'vacillations' was originally

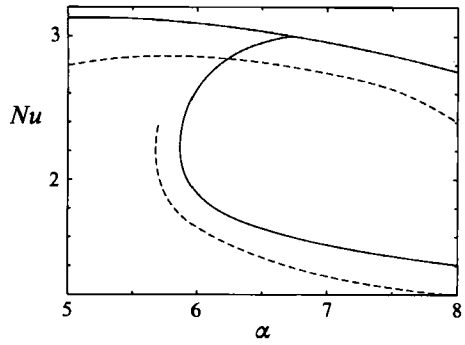

FIGURE 3. The dependence of the Nusselt number Nu on the wavenumber α for the cases $R = 2.5 \times 10^4, P = 0.7, \eta^* = 800$ (solid) and $R = 2.25 \times 10^4, P = 0.3, \eta^* = 1600$ (dashed). The bifurcating curves corresponds to mean flow convection. In the second case it has not been possible to continue the mean flow solution all the way to the bifurcation point.

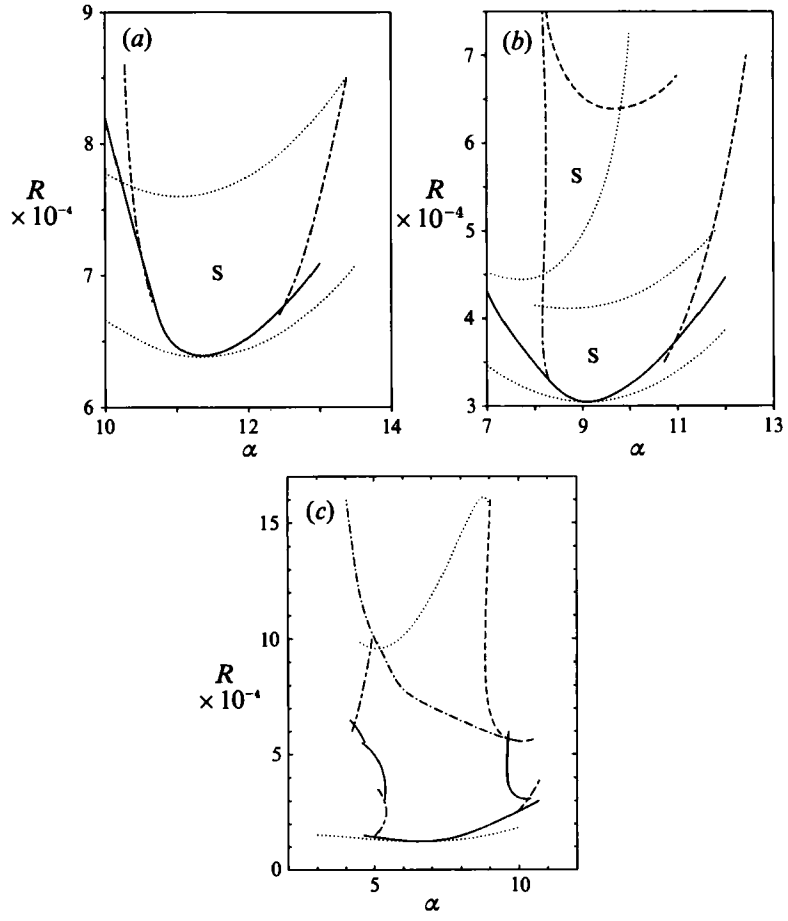

FIGURE 4. Stability regions of symmetric rolls (indicated by S) in the case of rigid boundaries with $P = 7$ for (*a*) $\eta^* = 2800$, (*b*) $\eta^* = 1600$ and (*c*) $\eta^* = 800$. The lowermost dotted curve indicates the neutral curve; the other dotted curve indicates the onset of vacillations. The dashed curve indicates the onset of the mean flow instability. Solid and double-dashed curves indicate various modes of sideband instability. In (*c*) the dash-dotted curve indicates the extent to which finite-amplitude mean flow convection coexists with stable symmetric convection rolls; i.e. subcriticality of the mean flow solution with respect to α occurs in this region.

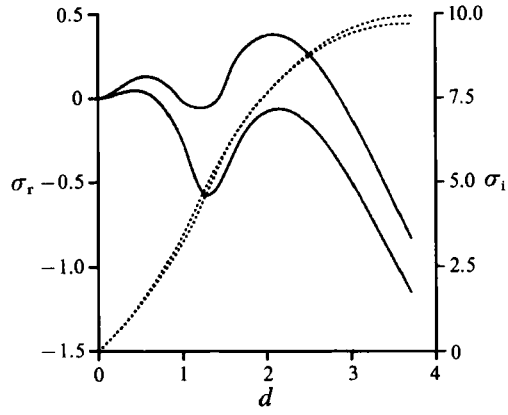

FIGURE 5. Real parts σ_r (solid lines) and imaginary parts σ_i (dotted lines) of sideband instabilities for $P = 7$, $\eta^* = 1600$, $R = 3.5 \times 10^4$. The lower lines correspond to $\alpha = 10.7$ the upper ones to $\alpha = 10.8$.

introduced in the case of the baroclinic annulus experiment (see, for example, Hide & Mason 1975). Typically, spatially averaged properties vary as much in time as the spatially fluctuating fields, in contrast to other wave phenomena.

As the rotation parameter η^* is decreased the stability boundaries change relatively little on the right-hand side of the diagram, but the vacillation instability begins to disappear for small wavenumber α as shown in figure 2(*b*) for $\eta^* = 1600$. At even lower values η^* the mean flow instability also becomes restricted to wavenumbers α exceeding the critical value α_c and the symmetric thermal Rossby waves remain stable up to at least ten times the critical value of the Rayleigh number if the wavenumber is located within a certain band below α_c. Thus the stability properties approach fairly smoothly the non-rotating limit of the problem for which no two-dimensional instability is known to restrict the range of stable convection rolls until much higher Rayleigh numbers.

When the mean flow convection solution is followed from its bifurcation point, it is found to exist at finite amplitude over wider range of α than suggested by the stability theory. In terms of increasing α the bifurcation occurs subcritically as indicated in figure 2(*c*). A more detailed picture of the bifurcation is shown in figure 3 where the Nusselt number has been plotted. This plot also demonstrates the sharp drop in the convective heat transport after the onset of the mean flow convection, which is caused by the fact that the convection velocity is diminished on one side of the layer and replaced by a nearly stagnant region which tends to impede the heat transport.

A similar set of stability diagrams for $P = 7.0$ instead of $P = 0.7$ is shown in figure 4. Here a vacillation-type instability precedes the transition to the mean flow solution in the cases $\eta^* = 2800$ and 1600. In the latter case the vacillating solution exists only for an intermediate range of Rayleigh numbers after which a return to symmetric thermal Rossby wave convection occurs at least for values of α less than the critical value. The case of $\eta^* = 800$ is characterized by an enlargement of the region of stable symmetric convection on the one hand and by a substantial subcritical region of finite-amplitude mean flow convection on the other hand as shown in figure 4(*c*).

It has already been apparent from the more limited analysis of OB87 that in addition to the Eckhaus instability, which restricts the wavenumber region for stable

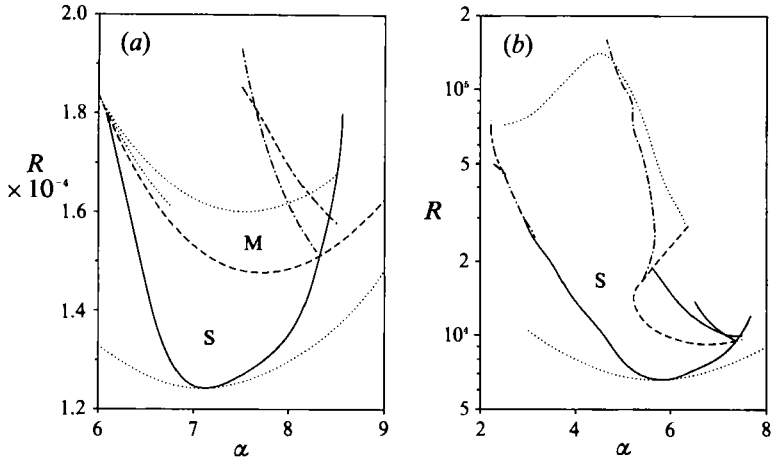

FIGURE 6. Stability regions of symmetric rolls (indicated by S) and of mean flow convection (indicated by M) in the case of rigid boundaries with $P = 0.3$ for (*a*) $\eta^* = 2800$ and (*b*) $\eta^* = 1600$. The lower dotted line indicates the neutral curve for onset of convection, the upper dotted line the onset vacillations; the intermediate dotted line in (*a*) indicates the onset of vacillations in the absence of mean flow convection and has been computed only for a short range of wavenumbers α. The long dash-dotted line in (*b*) indicates the extent (towards low wavenumbers α) to which finite-amplitude mean flow convection coexists with stable symmetric rolls. The other dash-dotted curves and the solid curves indicate various sideband instabilities.

rolls close to the critical Rayleigh number, there exist other sideband mechanisms of instability which set in with finite values of d. From the stability boundaries shown in figures 2 and 4 it is evident that quite a few distinguishable sideband instabilities restrict the region of stable symmetric convection or mean flow convection toward high and low values of α. The growth rates σ_r of these instabilities often correspond to multiple maxima of the same eigenvalue as a function of d as shown in figure 5. For a semi-analytical treatment of these modes we refer to Or (1990).

In figure 6 two stability diagrams for the case $P = 0.3$ are shown which resemble in their qualitative aspects those obtained for $P = 0.7$ in the cases $\eta^* = 800$. In contrast to the results of OB87 for periodic boundary conditions the mean flow instability remains the predominant instability over a large interval of the parameter η^*.

4. Vacillating convection

The vacillation instability reaches its maximum growth rate at a finite value of d. But since this value of d is usually relatively small and since the growth rate for $d = 0$ approaches the maximum value closely, it is justified to consider the case $d = 0$. In applications to laboratory experiments the case $d = 0$ may actually be preferred because only discrete values of d are permitted in an annulus with finite ratio D/r_0. The assumption $d = 0$ leads to a significant simplification of the numerical solution of the system of ordinary differential equations in time for the coefficients $\hat{a}_{mn}$, $\check{a}_{mn}$, $\hat{b}_{mn}$, $\check{b}_{mn}$. Forward integrations in time have been performed primarily for the case of periodic boundary conditions (2.7) that has already been considered in OB87.

After short transients the solutions exhibit periodic variations in the absolute values of $|\hat{a}^2_{mn} + \check{a}^2_{mn}|$ which are typical for vacillation phenomena. The period-doubling sequence found in OB87 has been confirmed. The fact that the truncation

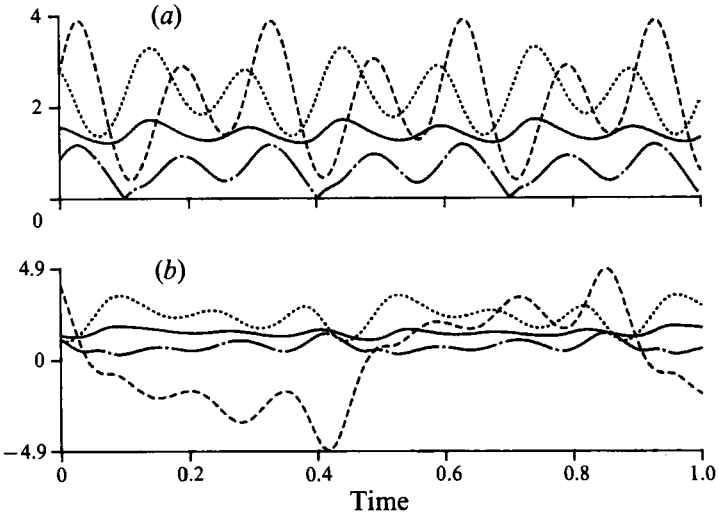

FIGURE 7. Time dependence of the Nusselt number (solid), of the coefficient $\hat{a}_{10}$ (dashed) of $\hat{a}_{11}^2+\check{a}_{11}^2$ (dotted), and of $\hat{a}_{12}^2+\check{a}_{12}^2$ (dash-dotted) for (*a*) $R = 38400$ and (*b*) $R = 38900$ in the case of periodic boundary conditions with $P = 1$, $\alpha = 9.4$, $\eta^* = 2800$.

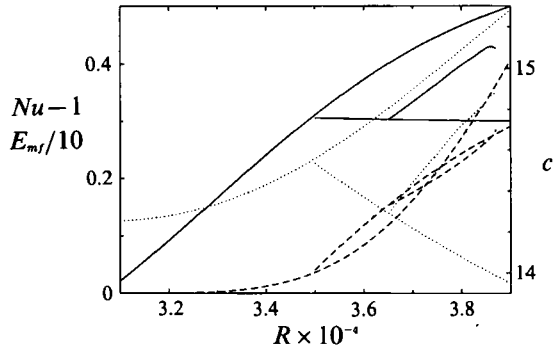

FIGURE 8. Nusselt number Nu (solid), drift rate c (dotted), and kinetic energy E_{mf} of the mean component of motion (dashed) as a function of the Rayleigh number for periodic boundary conditions with $P = 1$, $\alpha = 9.4$, $\eta^* = 2800$. The first point of bifurcation at $R = 35 \times 10^3$ corresponds to the onset of mean flow convection, the second bifurcation corresponds to the onset of vacillations. The kinetic energy of the fluctuating component of motion exhibits the same dependence on R as Nu-1 except it is larger by a factor of about 200.

parameter $N_T = 6$ has been used in place of $N_T = 4$ used in OB87 causes only a minor shift towards higher values of the Rayleigh numbers at which the bifurcations occur. In figure 7 the time dependence of some typical coefficients is displayed. The first period doubling occurs for $37500 < R < 38000$; at $R = 38400$ a quadrupling has taken place and at $R = 38500$ a further doubling has occurred. Soon thereafter chaotic solutions are found as expected according to the Feigenbaum scenario. In these vacillating solutions the convection appears to oscillate between a nearly symmetric state as indicated by small values of coefficients $|\hat{a}_{mn}|$ with odd $m+n$ and a state exhibiting the properties of the mean flow solution.

Since there are two mean flow solutions there are also two types of vacillating solutions differing by the sign of the coefficients $\hat{a}_{mn}$, $\check{a}_{mn}$ with odd $m+n$. In the chaotic region at a Rayleigh number of about 38600 and beyond these two types are intermingled and some of the time-periodic solutions which appear as windows

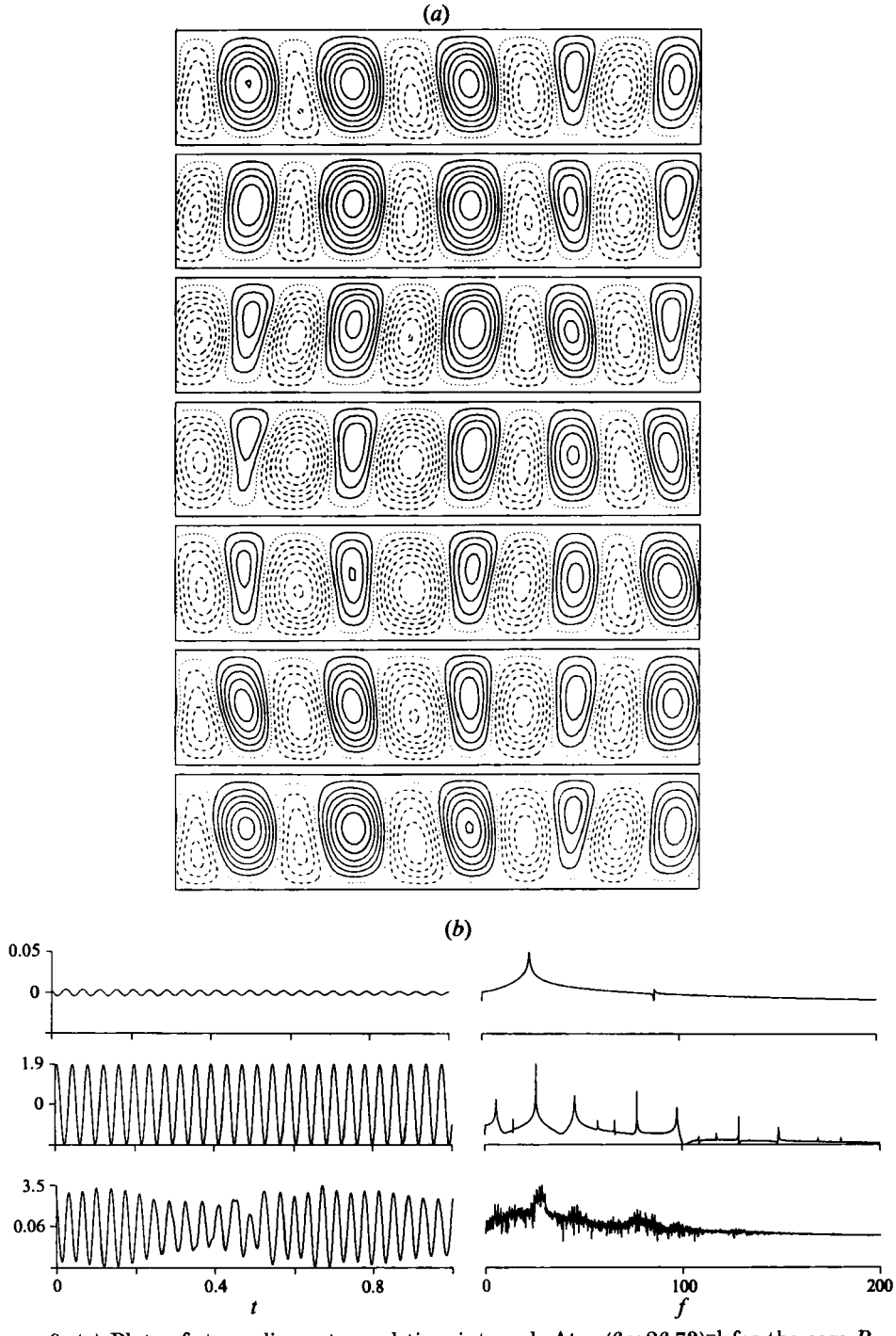

FIGURE 9. (*a*) Plots of streamlines at equal time intervals $\Delta t = (6 \times 26.73)^{-1}$ for the case $P = 0.7$, $\eta^* = 800, R = 7 \times 10^4, \alpha = 6$ with rigid boundaries. The streamlines are seen in the frame of reference drifting with the speed $c = 15.98$, such that the position of the rolls remains steady. While the plots cover a full period of the primary frequency (see *b*), the last plot differs from the first one because of contributions from other frequencies. (*b*) Time dependence of the coefficient $\hat{a}_{10}$ and corresponding Fourier spectrum (total range is 5 decades) for the same case as (*a*) with $R = 4.5 \times 10^4$, $R = 6 \times 10^4$, and $R = 7.5 \times 10^4$ (from top to bottom).

within this region show a periodic alteration between the two signs as shown in the example in figure 7(*b*). At higher values of the Rayleigh number windows of periodic solutions with a single sign of the coefficients $\hat{a}_{mn}$, $\check{a}_{mn}$ predominate again.

A main physical cause for the onset of vacillations appears to be the decrease with increasing Rayleigh number of the convective heat transport associated with mean flow convection. Because the amplitude of the latter is stronger on one side of the convection layer than on the other, an extended thermal boundary layer is needed at the opposite side to carry the heat flux. The buoyancy stored in this layer is converted by the vacillations into an increase of the kinetic energy of motion as is evident from figure 8. Similarly the drift rate of the rolls which decreases after the onset of the mean flow convection owing to a reduced stretching of vortex lines, increases again after the onset of vacillations as convection reoccupies the entire layer.

For smaller values of η^* the maximizing Floquet parameter d_m tends to increase and a study of vacillating convection based on the assumption $d = 0$ becomes less appropriate. In order to accommodate the evolving spatially modulated vacillating solutions within the representation (2.5) with time-dependent coefficients, a new wavenumber $\hat{\alpha} = \alpha/M$ has been defined, where M is a small natural number, say $2 \leqslant M \leqslant 6$. By selecting values of M close to α/d_m and by replacing the truncation condition (2.9) by

$$m+n/M > N_T \tag{4.1}$$

we have been able to solve the time-dependent equations for the coefficients $a_{mn}(t)$ in the case when $\hat{\alpha}$ has replaced α in the representation (2.5). These computations have been carried out primarily in the case of rigid boundaries because the values of d_m are especially favourable in this case. It is expected that no significant differences will appear when other boundary conditions are used.

An example of spatially modulated vacillating convection is shown in figure 9. The modulation assumes the form of a local depression of the amplitude of convection which propagates relative to the convection pattern. We note that the azimuthal scale of the streamline plots in this and in later figures has been stretched in order to better visualize some of the details. As the Rayleigh number is increased the spectrum of frequencies in the time series of a typical coefficient, say $\hat{a}_{10}$, becomes more complex and finally the time dependence becomes chaotic as shown in figure 9(*b*). This state exists only over a limited range of Rayleigh numbers. In the example of figure 9(*b*) convection returns to a periodically vacillating state with the wavenumber $\alpha = 4.8$ instead of $\alpha = 6.0$ when R reaches 7.6×10^4. The rearrangement of the convection rolls into a spatially periodic pattern with a somewhat larger wavelength offered by the computational scheme appears to be typical in all cases that have been investigated.

The technique of enlarging the wavenumber spectrum in order to include small but finite values of d_m has also been employed in the case of some of the sideband instabilities. As expected from the case of the Eckhaus instability the evolution of these instabilities leads to the establishment of a stationary solution with a wavenumber $\alpha = \alpha \pm d_m$ in the stable region.

5. Convection in the presence of curved end surfaces

The special case $\epsilon = 0$ of equations (2.3) considered in the preceding section has permitted the inversion symmetry of symmetric thermal Rossby waves which manifests itself in the vanishing of all coefficients $\hat{a}_{mn}$, $\check{a}_{mn}$, $\hat{b}_{mn}$, $\check{b}_{mn}$ with odd $m+n$.

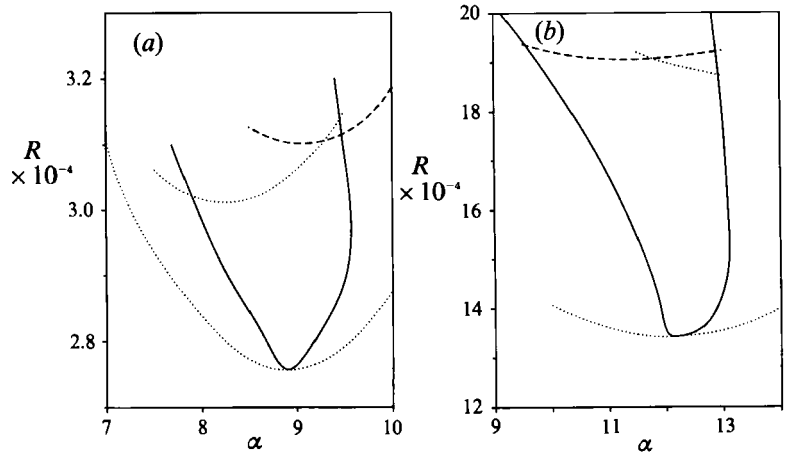

FIGURE 10. Stability boundaries of convection rolls in the case of curved end surfaces, $\epsilon = 1$: (*a*) rigid boundaries with $\eta^* = 2800$, $P = 0.7$; (*b*) periodic boundaries with $\eta^* = 10^4$, $P = 1$. The lower dotted curve indicates the onset of convection, the upper dotted curve the onset of vacillations, solid lines sideband instabilities and dashed lines the double-column instability.

This symmetry disappears as soon as finite values of ϵ are considered. As a consequence the bifurcation of the mean flow solution from the symmetric convection rolls can no longer be distinguished. It may be seen at most in the form of an imperfect bifurcation in the limit of small ϵ. On the other hand new effects can be expected. Since the characteristic frequency and wavenumber of convection rolls depend on η^*, the rolls tend to prefer different drift rates and even different wavelengths on the two sides of the layer if ϵ is sufficiently large. Indeed, one of the main results of the analysis is the breakup of the convection layer into two or more sublayers. In order to demonstrate these effects we shall focus attention on the case $\epsilon = 1$ in this section.

The onset of convection in the case $\epsilon = 1$ corresponds to rolls which are mostly confined to the inner, i.e. $x < 1$, part of the layer. As the Rayleigh number increases they become unstable with respect to the vacillation instability or with respect to the double-column instability, so named in OB87 because of the tendency of the disturbances to create a second row of rolls in the outer part of the layer. In the stability diagrams of figure 10 it is evident that both instabilities are in close competition with the vacillations preceding the onset of double columns in the case of rigid boundaries while the opposite situation prevails in the case of periodic boundary conditions. Similar stability diagrams are found for other values of η^* for which we refer to Schnaubelt (1992).

In OB87 the evolution of the double-column instability was studied numerically by introducing two sets of representations (2.5) into the basic equations, each with its own characteristic wavenumber, and by using common mean field coefficients $\hat{a}_{m0}$, $\hat{b}_{m0}$. The quality of this mean field approximation can now be tested through the use of the scheme developed for the computations of modulated convection. Since the double-column instability is characterized by relatively large values of d of the order of $\frac{1}{3}\alpha$ or even $\frac{1}{2}\alpha$ the computations can be carried out up to quite high values of the truncation parameter N_T in condition (4.1). A typical case of double-column convection is shown in figure 11 where the set of rolls in the lower part of each plot propagates relative to the row of rolls in the upper part, best seen in the left part of the figure in which the mean zonal component of ψ has been omitted. A detailed

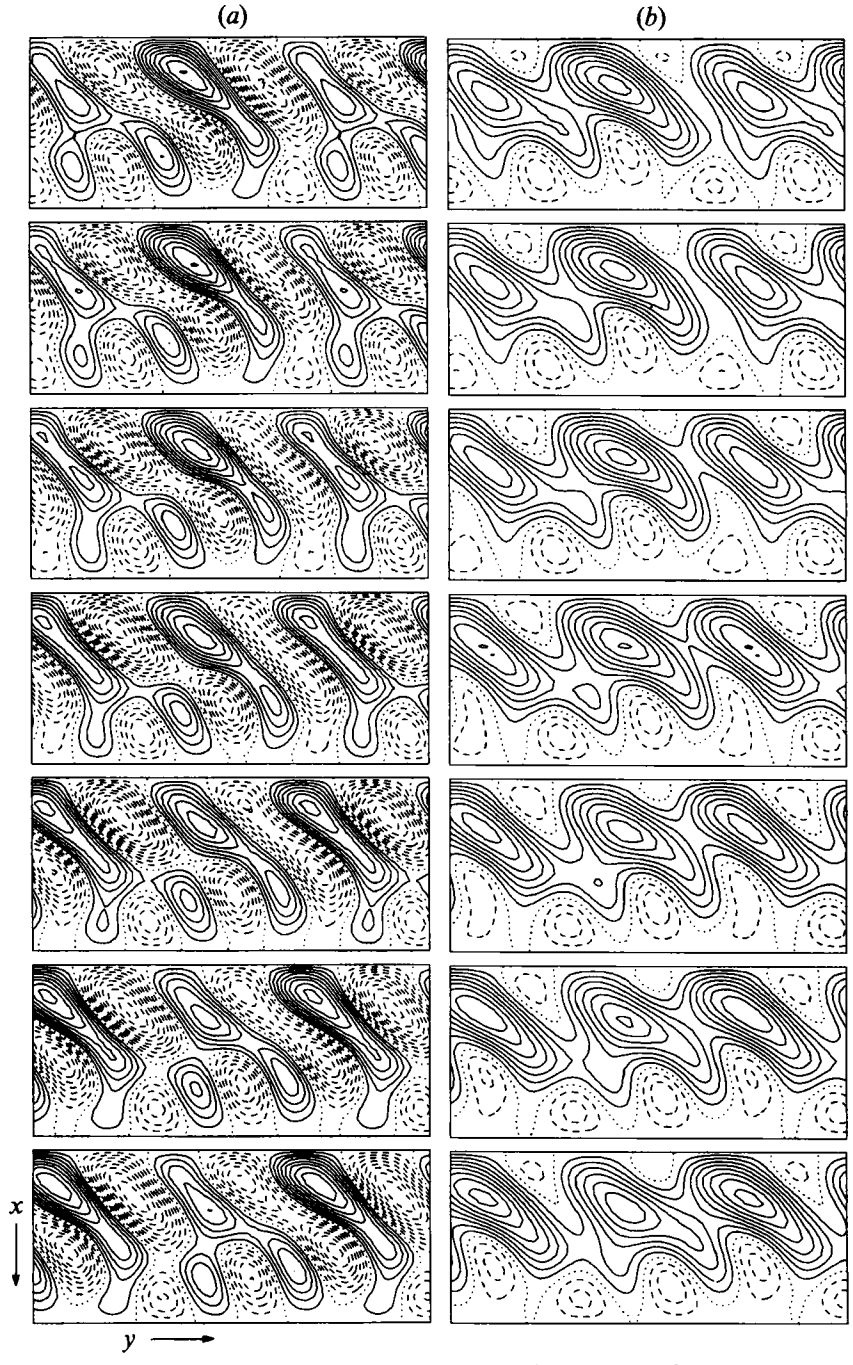

FIGURE 11. Plots of streamlines at equal time intervals $\Delta t = 2.8 \times 10^{-3}$ for the case $P = 1$, $\epsilon = 1$, $\eta^* = 10^4$, $\alpha = 10.5$, $R = 2 \times 10^5$ with periodic boundary conditions. Approximately one half-period has been covered. The stream function with y-average subtracted is shown in column (a), the total stream function is shown in (b). The reference frame propagates with the drift rate $c = 15.73$ of the inner convection rolls which thus remain fixed in position.

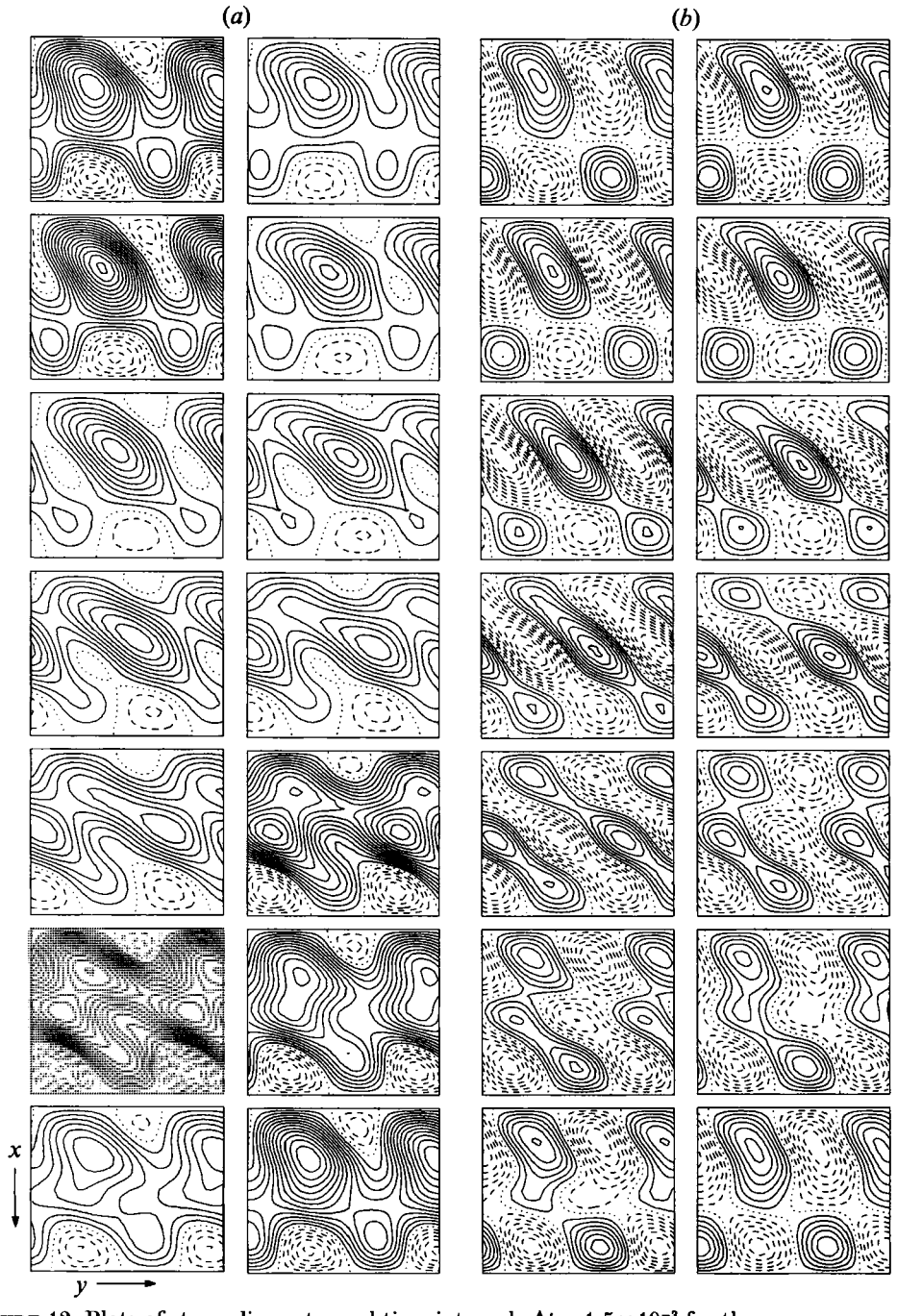

FIGURE 12. Plots of streamlines at equal time intervals $\Delta t = 1.5 \times 10^{-3}$ for the same case as figure 11, but with $R = 2.3 \times 10^5$, $c = 8.43$. Columns (*a*) show the total stream function while the y-average of the stream function has been subtracted in columns (*b*). In each case the time sequence is from top to bottom in the first column, then in the second column.

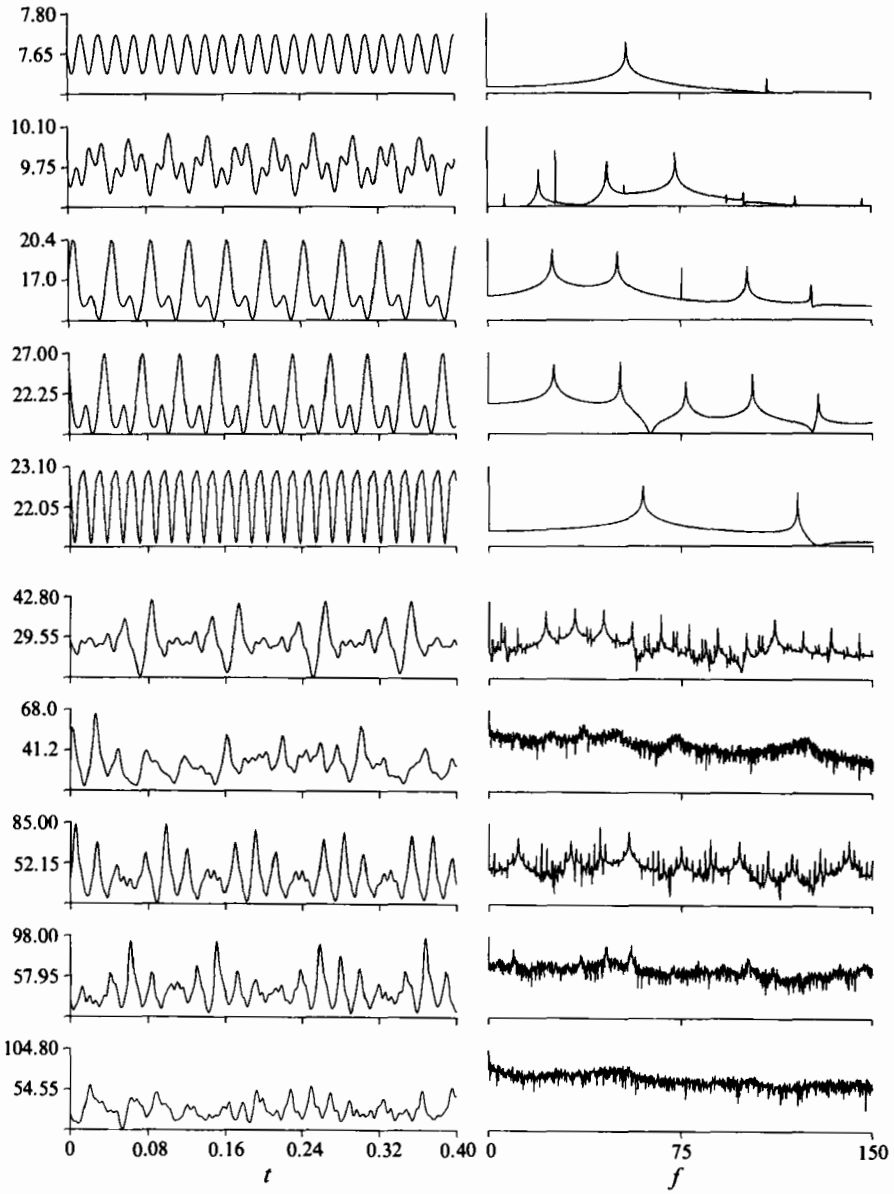

FIGURE 13. Time dependence of the coefficient $\hat{a}_{10}$ and corresponding spectra at ten Rayleigh numbers with equal increments of 10^4 between 2×10^5 and 2.9×10^5 for $P=1$, $\eta^*=10^4$, $\epsilon=1$, $\alpha=10.5$, $\hat{\alpha}=\frac{1}{2}\alpha$. The spectra are obtained from records continuing up to $t=8.0$ and the logarithmic scale of the spectra extends over 5 decades.

inspection of the coefficients indicates that those corresponding to $m=pM$ and to $m=p(M+1)$, $p=0,1,2,\ldots$ predominate in comparison to others and are nearly constant in time as must be expected for two nearly independent thermal Rossby waves. This property supports the assumption made in the analysis of OB87 where $\alpha_1=M\hat{\alpha}$ and $\alpha_2=(M+1)\hat{\alpha}$ have been used, albeit at a different place in the parameter space. Only as the Rayleigh number is increased further, do interaction coefficients other than mean field coefficients become important.

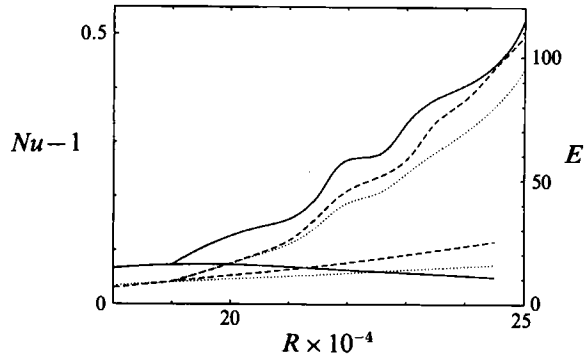

FIGURE 14. Nusselt number, Nu-1 (solid), kinetic energy of the mean component (dashed), and of the fluctuating component (dotted, right ordinate multiplied by factor 4) as a function of the Rayleigh number for $P = 1$, $\epsilon = 1$, $\eta^* = 10^4$, $\alpha = 10.5$ with periodic boundary conditions.

At the Rayleigh number 2.3×10^5 the convection state returns to the single wavenumber $\alpha = 10.5$, i.e. the second thermal Rossby wave adjusts its wavenumber to that of the first thermal Rossby wave, but they still propagate relative to each other as shown in figure 12. In this particular case a division of the layer into three sublayers is noticeable, in which convection rolls in the centre are combined in an alternating fashion with the outer and the inner row of convection rolls. The interlude of a singly spatially periodic pattern gives way to a more complex pattern at a higher Rayleigh number of the order 2.4×10^5 where all coefficients offered in the scheme assume finite amplitudes. This development quickly leads to a chaotic time dependence as shown in figure 13 where some of the transitions can be recognized in the Fourier spectra.

The onset of the second row of convection rolls leads to a strong increase of the convective heat transport and of the kinetic energies of various components as shown in figure 14. Even as the time dependence becomes aperiodic the rate of increase of these quantities does not diminish.

6. Discussion

Convection induced by centrifugal buoyancy in a rotating annulus with finite η^* shares with convection in a layer heated from below and rotating about a vertical axis the property that the reflection symmetry in the azimuthal direction is lost. In the annulus problem this loss manifests itself in the azimuthal drift of convection columns and in the phase shift between the radial velocity component and the temperature. The phase shift causes subsequent bifurcations which are absent in the case $\eta^* = 0$. The dynamic phenomena exhibited by two-dimensional convection in an annulus are thus as rich as those characterizing three-dimensional convection in layers heated from below, but they are much more accessible to numerical analysis.

In the preceding section some typical dynamic feature have been described and the prominent role of mean zonal flow has been emphasized. The tendency of the convection layer to break into several layers of convection rolls propagating at their own speed is the most interesting result of this analysis. This property lends support to the model of Busse (1976, 1983) of a sequence of five cylindrical layers in the equatorial region of the Jovian atmosphere. As was noted in OB87, a number of other features of annulus convection appear to be related to observations on Jupiter, such as the cyclonic nature of the convection eddies as seen, for example, in figure 11.

There is little theoretical evidence for the relatively large azimuthal wavelengths of the small cyclonic features in the Jovian atmosphere such as the brown barges or the cores of the north equatorial plumes. Perhaps isolated convection columns embedded in regions of more or less quiescent fluid will become a typical phenomenon at much higher Rayleigh number than those reached in the present analysis.

A most interesting property of vacillating convection is the strong increase in the heat transport in comparison with steadily drifting rolls. This property contrasts with usual decrease of the convective heat transport after the onset of the oscillatory instability in the case of a non-rotating Rayleigh–Bénard layer. The conservation of angular momentum tends to suppress the radial component of flow and time-dependent processes are obviously more efficient to overcome this constraint of rotation. In the particular case of the annulus the low heat transport by the mean flow convection is caused by the nearly stagnant region that develops near the inner or near the outer boundary. The onset of vacillations disrupts this stagnant layer and thus leads to an increase of the heat transport. Since the region of parameter space that has been explored by numerical computations is still rather limited, detailed observations of time-dependent processes in experiments or on Jupiter will be helpful to learn more about the mechanisms which contribute to an effective convective heat transport.

A new generation of laboratory annulus experiments appears to be desirable, because values of η^* realized in previous experiments (Busse & Carrigan 1976; Busse & Hood 1982; Azouni, Bolton & Busse 1985) did not exceed a few hundred. Although the comparisons with the predictions of linear theory show reasonable quantitative agreement, the experimental observations of nonlinear effects have remained at a qualitative level. In order to reach the physically interesting region of $\eta^* \approx 10^3$ or more, larger gap widths and higher rotation rates are needed than have been used in the past. It is hoped that some of the interesting phenomena seen in the numerical simulations will inspire experimental fluid dynamicists to adopt the rotating annulus experiment as a tool for basic research.

The research reported in this paper has been supported by the Deutsche Forschungsgemeinschaft under grant BU589/2-1.

REFERENCES

Azouni, A., Bolton, E. W. & Busse, F. H. 1986 Experimental study of convection columns in a rotating cylindrical annulus. *Geophys. Astrophys. Fluid Dyn.* **34**, 301–317.

Brummell, N. H. & Hart, J. E. 1992 High Rayleigh number β-convection. *Geophys. Astrophys. Fluid Dyn.* (in press).

Busse, F. H. 1970 Thermal instabilities in rapidly rotating system. *J. Fluid Mech.* **44**, 441–460.

Busse, F. H. 1976 A simple model of convection in the Jovian atmosphere. *Icarus* **20**, 255–260.

Busse, F. H. 1982 Thermal convection in rotating systems. In *Proc. Ninth US Natl Congr. of Applied Mechanics*, pp. 299–305. ASME.

Busse, F. H. 1983 A model of mean zonal flow in the major planets. *Geophys. Astrophys. Fluid Dyn.* **23**, 153–174.

Busse, F. H. 1984 Transition to turbulence via the statistical limit cycle route. In *Turbulence and Chaotic Phenomena in Fluids* (ed. by T. Tatsumi), pp. 197–202. Elsevier.

Busse, F. H. 1986 Asymptotic theory of convection in a rotating, cylindrical annulus. *J. Fluid Mech.* **173**, 545–556.

Busse, F. H. & Carrigan, C. R. 1974 Convection induced by centrifugal buoyancy. *J. Fluid Mech.* **62**, 579–592.

BUSSE, F. H. & CLEVER, R. M. 1979 Nonstationary convection in a rotating system. In *Recent Developments in Theoretical and Experimental Fluid Mechanics* (ed. U. Müller, K. G. Roesner & B. Schmidt), pp. 376–385. Springer.

BUSSE, F. H. & HEIKES, K. E. 1980 Convection in a rotating layer: A simple case of turbulence. *Science* **208**, 173–175.

BUSSE, F. H. & HOOD, L. L. 1982 Differential rotation driven by convection in a rotating annulus. *Geophys. Astrophys. Fluid Dyn.* **21**, 59–74.

CHANDRASEKHAR, S. 1961 *Hydrodynamic and Hydromagnetic Stability*. Clarendon.

HIDE, R. & MASON, P. J. 1975 Sloping convection in a rotating fluid. *Adv. Phys.* **24**, 47–100.

KÜPPERS, G. & LORTZ, D. 1969 Transition from laminar convection to thermal turbulence in a rotating fluid layer. *J. Fluid Mech.* **35**, 609–620.

OR, A. C. 1990 New phenomena in the Eckhaus instability of thermal Rossby waves. *J. Fluid Mech.* **216**, 613–628.

OR, A. C. & BUSSE, F. H. 1987 Convection in a rotating cylindrical annulus. Part 2. Transitions to asymmetric and vacillating flow. *J. Fluid Mech.* **174**, 313–326 (referred to herein as OB87).

SCHNAUBELT, M. 1992 Stationäre und zeitabhängige Konvektion im rotierenden zylindrischen Annulus. Dissertation, University of Bayreuth.

SCHNAUBELT, M. & BUSSE, F. H. 1990 Convection in a rotating cylindrical annulus with rigid boundaries. In *Nonlinear Evolution of Spatio-Temporal Structures in Dissipative Continuous Systems* (ed. F. H. Busse & L. Kramer), pp. 67–72. Plenum NATO Series.